Mechanical Properties of Zr–Si–N Films Fabricated through HiPIMS/RFMS Co-Sputtering

Li-Chun Chang [1,2,*], Yu-Zhe Zheng [3] and Yung-I Chen [3]

[1] Department of Materials Engineering, Ming Chi University of Technology, New Taipei City 24301, Taiwan
[2] Center for Plasma and Thin Film Technologies, Ming Chi University of Technology, New Taipei City 24301, Taiwan
[3] Institute of Materials Engineering, National Taiwan Ocean University, Keelung 20224, Taiwan; 10555014@ntou.edu.tw (Y.-Z.Z.); yichen@mail.ntou.edu.tw (Y.-I.C.)
[*] Correspondence: lcchang@mail.mcut.edu.tw; Tel.: +886-2-2908-9899

Abstract: Zr–Si–N films were fabricated through the co-deposition of high-power impulse magnetron sputtering (HiPIMS) and radio-frequency magnetron sputtering (RFMS). The mechanical properties of the films fabricated using various nitrogen flow rates and radio-frequency powers were investigated. The HiPIMS/RFMS co-sputtered Zr–Si–N films were under-stoichiometric. These films with Si content of less than 9 at.%, and N content of less than 43 at.% displayed a face-centered cubic structure. The films' hardness and Young's modulus exhibited an evident relationship to their compressive residual stresses. The films with 2–6 at.% Si exhibited high hardness of 33–34 GPa and high Young's moduli of 346–373 GPa, which was accompanied with compressive residual stresses from −4.4 to −5.0 GPa.

Keywords: HiPIMS; mechanical properties; residual stress; RFMS

1. Introduction

Nanocomposite nitride films are comprised of nacocrystalline metal–nitride grains scattered in an amorphous Si_3N_4 matrix. These are recognized as $nc\text{-}Me_nN/a\text{-}Si_3N_4$ films, and have been widely investigated [1–4]. A hardness of 50 GPa was attained for $nc\text{-}TiN/a\text{-}Si_3N_4$ films, which was attributed to the inhibition of crack propagation by the amorphous tissue surrounding the nanocrystals [1]. The Ti–Si–N films with 8 at.% Si exhibited maximum hardness [1,2]. Previous studies [5–7] have applied the $nc\text{-}Me_nN/a\text{-}Si_3N_4$ model to interpret the hardness improvement of Nb–Si–N films, which exhibited a hardness of 34 GPa accompanied with the addition of 5–13 at.% Si. However, the hardness enhancement for Nb–Si–N films is restricted in contrast to that for Ti–Si–N films. Moreover, the previous works on Zr–Si–N films [8–11] also exhibited restricted improvement in hardness as the addition of 2–6 at.% Si achieved a hardness of 30–36 GPa. Additionally, the reported strengthening mechanisms were not consistent. The $nc\text{-}Me_nN/a\text{-}Si_3N_4$ model could not be applied to most Si-containing metal-nitride films. In our previous studies on Ta–Si–N [12], Nb–Si–N [13] and Zr–Si–N [14] coatings, fabricated using direct-current magnetron sputtering (DCMS) (introducing high Si contents into nitrides), formed an amorphous structure on X-ray and improved the oxidation resistance; although their mechanical properties deteriorated. Therefore, high-Si-content Ta–Si–N [15] and Zr–Si–N [16] coatings are applied for glass molding dies, which are operated under a low oxygen-containing atmosphere at approximately 600 °C. By contrast, the low-Si-content Zr–Si–N coatings exhibited a crystalline structure accompanied with a hardness level of 23–24 GPa and a compressive stress of less than 2 GPa [14]. High-power impulse magnetron sputtering (HiPIMS) [17,18] was recommended to grow films with a dense structure, high hardness and high

residual compressive stress [19,20]. Therefore, exploring the mechanical performance of low-Si-content Zr–Si–N films fabricated by HiPIMS is essential for extending potential practical applications. Because the HiPIMS process resulted in low deposition rates [18], hybrid HiPIMS/DCMS [21] and HiPIMS/RFMS (radio-frequency magnetron sputtering) [22] were utilized to raise the deposition rate. In a previous study [23], the ZrN_x films prepared using HiPIMS system exhibited a nanoindentation hardness level of 26–27 GPa. In this study, Zr–Si–N films were fabricated through HiPIMS/RFMS hybrid process, before the mechanical properties of these films were investigated.

2. Materials and Methods

Figure 1 shows the schematic of HiPIMS/RFMS co-sputtering system. A target of 99.999% pure Si was connected to a RF (radio-frequency) power generator (13.56 MHz), while the targets of 99.995% Ti and 99.9% Zr were connected to a pulse power supply (SPIK 2000A; Shen Chang Electric Co., Ltd., Taipei, Taiwan) operated in the unipolar negative mode. The Si, Ti, and Zr targets were 50.8, 76.2 and 76.2 mm in diameter, respectively. The chamber was pumped to a base pressure of 6.7×10^{-4} Pa using a turbopump (TURBOVAC 600C, Leybold, Hsinchu, Taiwan) and monitored by an ionization gauge (274005, Granville-Phillips Company, Longmont, CO, USA). The substrate-to-target distance was 12 cm. The substrate holder without heating was rotated at 10 rpm and was grounded. The substrate holder was maintained at less than 70 °C during the deposition, which resulted in an insignificant thermal stress of less than 0.1 GPa. A working pressure of 0.4 Pa was formed after introducing 30-sccm-Ar flow into the chamber, before Ti was deposited at 400 W for 40 min. This creates an interlayer on silicon substrates, which had a thickness of 80–100 nm. Subsequently, Zr–Si–N films were co-sputtered on Ti interlayers after flowing a gas mixture of Ar and N_2 into the chamber. The sum of the Ar and N_2 flow rates were maintained at 30 sccm and the working pressure was maintained at 0.4 Pa. The HiPIMS process was conducted using the pulse on-time (t_{on}) and pulse off-time (t_{off}) of 100 and 3900 μs, respectively, which resulted in a duty cycle of 2.5% and a repetition frequency of 250 Hz. Table 1 lists the main variables for depositing Zr–Si–N films. Batch I samples were prepared using various nitrogen flow rates, while Batch II samples were prepared using various sputter powers. The chemical compositions of the films were analyzed using a field-emission electron probe microanalyzer (FE-EPMA, JXA-8500F, JEOL, Akishima, Japan). The PET (pentaerythritol), TAP (Thallium acid phthalate), and LDE1 (layered diffracting elements of W and Si) crystals were used to analyze Zr, Si, as well as N, and O, respectively. The samples were labeled as $Zr_xSi_yN_{100-x-y}$. The film thicknesses determined on the fracture surface were evaluated by field emission scanning electron microscopy (FE-SEM, S4800, Hitachi, Tokyo, Japan). Grazing-incident X-ray diffraction (GIXRD) was performed by using an X-ray diffractometer (XRD, X'Pert PRO MPD, PANalytical, Almelo, The Netherlands) to identify the phases. The incidence angle was 1°. Moreover, the XRD patterns were obtained by the Bragg–Brentano (θ–2θ) scan to calculate lattice parameters and texture coefficients. The nanostructure of the films was observed using transmission electron microscopy (TEM, JEM-2010F, JEOL, Akishima, Japan). The TEM samples with a protective Pt layer were produced using a focused ion beam system (FEI Nova 200, Hillsboro, OR, USA). The mechanical properties, hardness and Young's modulus of the films were evaluated using a nanoindentation tester (TI-900 Triboindenter, Hysitron, Minneapolis, MN, USA) and calculated using the Oliver and Pharr method [24]. An atomic force microscope (AFM, DI 3100, Bruker, Santa Barbara, CA, USA) recorded the surface roughness. The residual stress of the films was measured by the curvature method [25].
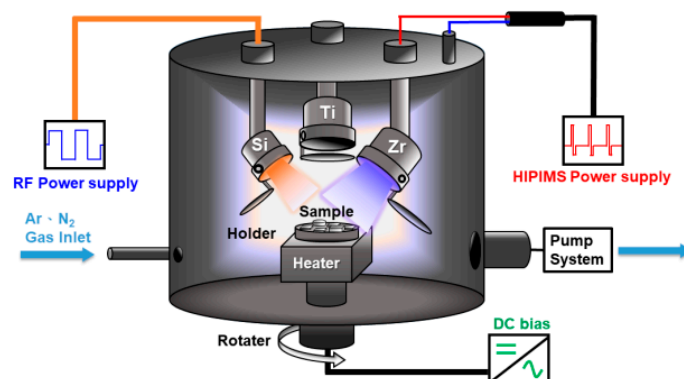
Figure 1. Schematic of the high-power impulse magnetron sputtering (HiPIMS) and radio-frequency magnetron sputtering (RFMS) co-sputtering equipment.

Table 1. Sputtering parameters and thicknesses of Zr–Si–N films.

Sample	Ar (sccm)	N_2 (sccm)	HiPIMS Power W_{Zr} (W)	RF Power W_{Si} (W)	Ave. Target Voltage (V)	Peak Current (A)	Time (min)	Thickness (nm)	Rate (nm/min)
				Batch I					
$Zr_{52}Si_8N_{40}$	28.0	2.0	300	50	660	67	210	831	4.0
$Zr_{48}Si_9N_{43}$	27.5	2.5	300	50	643	80	200	720	3.6
$Zr_{45}Si_{10}N_{45}$	27.0	3.0	300	50	600	90	240	732	3.0
$Zr_{44}Si_{10}N_{46}$	26.5	3.5	300	50	588	105	310	836	2.7
$Zr_{43}Si_{10}N_{47}$	26.0	4.0	300	50	588	110	360	898	2.5
				Batch II					
$Zr_{71}N_{29}$	28.0	2.0	300	0	640	58	400	1183	3.0
$Zr_{62}Si_2N_{36}$	28.0	2.0	300	25	618	67	285	937	3.3
$Zr_{62}Si_3N_{35}$	28.0	2.0	300	30	617	50	270	932	3.4
$Zr_{58}Si_5N_{37}$	28.0	2.0	300	35	615	70	255	926	3.6
$Zr_{56}Si_6N_{38}$	28.0	2.0	300	40	615	67	230	847	3.8
$Zr_{52}Si_8N_{40}$	28.0	2.0	300	50	660	67	210	831	4.0
$Zr_{50}Si_{10}N_{40}$	28.0	2.0	300	60	660	70	210	876	4.2

3. Results and Discussion

3.1. Zr–Si–N Films Fabricated Using Various Nitrogen Flow Rates

Table 2 shows the chemical compositions of the Batch I films fabricated using various nitrogen flow rates. The O contents of the Zr–Si–N films were in the range of 0.3–1.2 at.%. The N content of the films increased from 40 to 43, 45, 46, and 47 at.% when the nitrogen flow rate was increased from 2.0 to 2.5, 3.0, 3.5, and 4.0 sccm, respectively. The Si content was changed from 8 to 9, 10, 10, and 10 at.%, respectively. The film thickness was maintained at levels of 720–898 nm by adjusting the deposition times. Figure 2 exhibits an evident decrease in the deposition rate from 4.0 to 2.5 nm/min as the nitrogen flow rate is increased from 2.0 to 4.0 sccm. The decrease was attributed to the highly ionized reactive gas used in the HiPIMS process, which had a severe poisoning effect of the Zr target [26–28].

Table 2. Chemical compositions, surface roughness, mechanical properties and residual stress values of Zr–Si–N films.

Sample	Chemical Composition (at.%)				R_a (nm)	H^a (GPa)	E^b (GPa)	H^3/E^2 (GPa)	Stress ^{c} (GPa)
	Zr	Si	N	O					
Batch I									
$Zr_{52}Si_8N_{40}$	52.0 ± 1.1	7.6 ± 0.2	40.1 ± 1.3	0.3 ± 0.1	3.5 ± 0.1	27.4 ± 1.6	256 ± 7	0.31	−2.8 ± 0.1
$Zr_{48}Si_9N_{43}$	47.5 ± 0.7	9.0 ± 0.2	42.3 ± 0.9	1.2 ± 0.1	2.2 ± 0.2	20.4 ± 1.4	246 ± 9	0.14	−1.6 ± 0.2
$Zr_{45}Si_{10}N_{45}$	44.6 ± 1.1	10.2 ± 0.2	44.4 ± 1.0	0.8 ± 0.2	1.1 ± 0.1	14.5 ± 0.2	184 ± 3	0.09	−0.4 ± 0.1
$Zr_{44}Si_{10}N_{46}$	43.1 ± 1.3	10.1 ± 0.4	45.8 ± 1.3	1.0 ± 0.2	1.1 ± 0.1	13.8 ± 0.5	187 ± 7	0.08	−0.2 ± 0.1
$Zr_{43}Si_{10}N_{47}$	42.4 ± 1.3	10.0 ± 0.2	46.6 ± 0.9	1.0 ± 0.3	1.1 ± 0.4	14.0 ± 0.6	190 ± 8	0.08	−0.6 ± 0.1
Batch II									
$Zr_{71}N_{29}$	70.6 ± 0.5	0.1 ± 0.0	28.7 ± 0.7	0.6 ± 0.2	4.4 ± 0.2	21.5 ± 1.1	283 ± 13	0.12	−0.7 ± 0.1
$Zr_{62}Si_2N_{36}$	61.1 ± 1.9	2.2 ± 0.1	35.8 ± 2.1	0.9 ± 0.3	1.3 ± 0.2	33.1 ± 1.0	346 ± 11	0.30	−4.9 ± 0.3
$Zr_{62}Si_3N_{35}$	61.0 ± 0.4	3.2 ± 0.1	34.9 ± 0.4	0.9 ± 0.2	1.4 ± 0.1	34.4 ± 1.0	369 ± 11	0.30	−5.0 ± 0.4
$Zr_{58}Si_5N_{37}$	57.5 ± 0.2	4.5 ± 0.2	37.1 ± 0.1	0.9 ± 0.2	1.1 ± 0.0	34.0 ± 1.4	367 ± 13	0.29	−4.7 ± 0.2
$Zr_{56}Si_6N_{38}$	55.8 ± 0.2	5.6 ± 0.1	37.9 ± 0.3	0.7 ± 0.2	0.8 ± 0.1	33.2 ± 1.0	373 ± 12	0.26	−4.5 ± 0.6
$Zr_{52}Si_8N_{40}$	52.0 ± 1.1	7.6 ± 0.2	40.1 ± 1.3	0.3 ± 0.1	3.5 ± 0.1	27.4 ± 1.6	256 ± 7	0.31	−2.8 ± 0.1
$Zr_{50}Si_{10}N_{40}$	49.9 ± 0.6	9.7 ± 0.1	40.2 ± 0.8	0.2 ± 0.3	3.3 ± 0.0	21.5 ± 1.8	230 ± 7	0.19	−1.9 ± 0.1

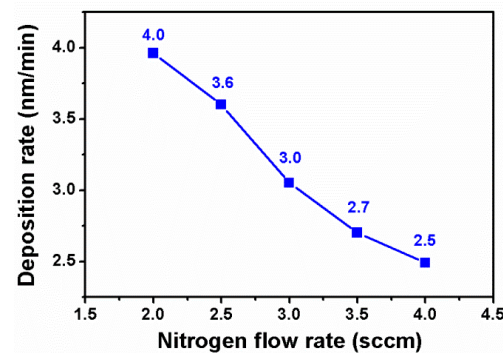^{a}: Hardness; ^{b}: Young's modulus; ^{c}: Residual stress.

Figure 2. Deposition rates of Batch I Zr–Si–N films fabricated using various nitrogen flow rates.

Figure 3 depicts the GIXRD patterns of the Zr–Si–N films. The $Zr_{52}Si_8N_{40}$ and $Zr_{48}Si_9N_{43}$ films displayed a face-centered cubic (fcc) ZrN (ICDD 35-0753) phase; the $Zr_{45}Si_{10}N_{45}$ films exhibited mixed fcc ZrN and X-ray amorphous phases; and the $Zr_{44}Si_{10}N_{46}$ and $Zr_{43}Si_{10}N_{47}$ films were found to have an X-ray amorphous phase. Although the differences in Si and N contents between these films were not large, the structure varied evidently. The films with Si content of less than 9 at.% and N content less than 43 at.% exhibited a fcc structure, while the films with Si and N contents above the limitations exhibited an amorphous phase-dominated structure.
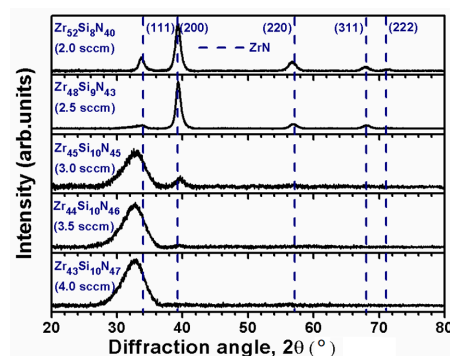

Figure 3. Grazing-incident X-ray diffraction (GIXRD) patterns of Zr–Si–N films fabricated using various nitrogen flow rates.

Table 2 lists the surface roughness, hardness, Young's modulus and residual stress values of Zr–Si–N films. The crystalline $Zr_{52}Si_8N_{40}$ and $Zr_{48}Si_9N_{43}$ films exhibited relatively high surface roughness levels (R_a) of 3.5 and 2.2 nm, respectively. The $Zr_{45}Si_{10}N_{45}$ films revealed the lowest roughness level of 0.3 nm, while the amorphous $Zr_{44}Si_{10}N_{46}$ and $Zr_{43}Si_{10}N_{47}$ films exhibited a roughness level of 1.1 nm. Figure 4 shows the variations of hardness and residual stress related to different N_2 flow rates. The hardness values of crystalline $Zr_{52}Si_8N_{40}$ and $Zr_{48}Si_9N_{43}$ films were 27.4 and 20.4 GPa, respectively, which were accompanied with residual stress of −2.8 and −1.6 GPa, respectively. In contrast, the $Zr_{45}Si_{10}N_{45}$, $Zr_{44}Si_{10}N_{46}$ and $Zr_{43}Si_{10}N_{47}$ films exhibited a hardness level of 13.8–14.5 GPa, which was accompanied with the presence of an amorphous. This resulted in a low residual stress level of −0.2 to −0.6 GPa. The elastic moduli and hardness of Zr–Si–N films displayed similar variations related to their chemical compositions. Additionally, the H^3/E^2 values, which represent resistance to plastic deformation [29], were 0.31 and 0.14 GPa for the crystalline $Zr_{52}Si_8N_{40}$ and $Zr_{48}Si_9N_{43}$ films, respectively. By contrast, the $Zr_{45}Si_{10}N_{45}$, $Zr_{44}Si_{10}N_{46}$ and $Zr_{43}Si_{10}N_{47}$ films containing an amorphous phase exhibited a low H^3/E^2 level of 0.08–0.09 GPa.
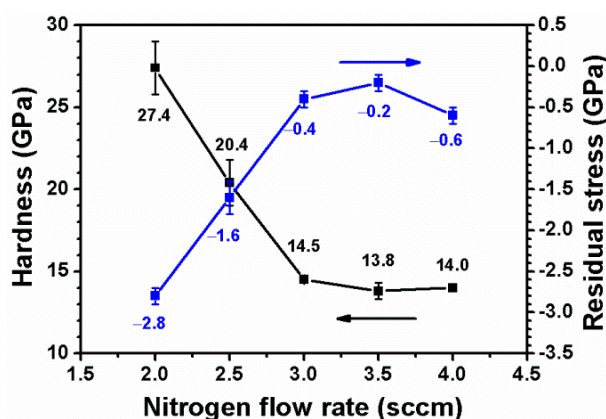

Figure 4. Nanoindentation hardness and residual stress values of Zr–Si–N films fabricated using various nitrogen flow rates.

3.2. Zr–Si–N Films Fabricated Using Various Power Levels

The Batch II films were fabricated through HiPIMS/RFMS co-sputtering using an average HiPIMS power of 300 W on the Zr target and various RF powers on the Si target (Table 1). The O contents of the films were 0.2–0.9 at.% (Table 2). The N content of the Batch II samples was changed from 29 to 36, 35, 37, 38, 40, and 40 at.% as the RF power increased from 0 to 25, 30, 35, 40, 50 and 60 W, respectively, and the Si content varied from 0, to 2, 3, 5, 6, 8, and 10 at.%, respectively. Both Batches I and II samples exhibited an atomic ratio N/(Zr + Si) of 0.41–0.89, which is under the stoichiometric ratio of 1.0 for ZrN. In a previous study [22], Ta–Zr–N films fabricated by the same HiPIMS/RFMS co-sputtering also exhibited an under-stoichiometric N/(Ta + Zr) ratio of 0.40–0.68. In another previous work [23], ZrN_x films prepared using HiPIMS system exhibited an under-stoichiometric N/Zr ratio of 0.65–0.78. The deposition times for Batch II processes were adjusted to fabricate films with similar thickness values of 831–1183 nm. The deposition rates increased from 3.0 to 4.2 nm/min when increasing the RF power from 0 to 60 W.

Figure 5 displays the GIXRD patterns of the Zr–Si–N films with various Si content. The $Zr_{71}N_{29}$ films exhibited a fcc ZrN structure with a strong (111) reflection. The introduction of Si into the films caused the structure to exhibit a strong (200) reflection, while the (111) reflection diminished. The fcc reflections became broadened and shifted toward the right side with further increases in the Si content in the films. Figures 6 and 7 show the XRD patterns under a Bragg–Brentano scan and their texture coefficients [30,31] of the Batch II films, respectively. The reflections of Ti [ICDD 44-1294], TiSi [ICDD 17-0424] and $ZrSi_2$ [ICDD 32-1499] phases were observed besides a ZrN phase. The Ti

and TiSi reflections were presented in another Ti/Si sample (not shown in this paper). The preferred orientations were (111) and (200) for the films with Si contents of <6 at.% and >8 at.%, respectively. Figure 8 exhibits the lattice parameters and grain sizes of the Zr–Si–N films calculated using (111) reflections. The lattice parameters decreased when increasing the Si content from 0 to 8 at.% due to the small atomic size of Si compared to Zr. This implied that 8 at.% Si or part of the 8 at.% Si was solved in the ZrN matrix and the residual Si atoms may reside at grain boundaries. Sandu et al. [7] suggested a solubility limit of 4 at.% Si for Nb–Si–N and Zr–Si–N films. A three-region model interpreted the structural evolution of composite M–Si–N films, which included the solubility of Si, coverage layer of SiN_x at grain boundaries and reduction of crystallite size. In contrast, the lattice parameters of the $Zr_{50}Si_{10}N_{40}$ films with a higher Si content of 10 at.% were larger than those of the films with 4–6 at.% Si, which could be attributed to the coexistence of Zr_3N_4 [16]. The grain sizes of the Batch II films determined by the Scherrer formula [32] exhibited a decreasing trend from 19.8 to 17.3, 17.7, 10.6 and 8.1 nm when increasing the Si contents from 0 to 3, 6, 8 and 10 at.%.
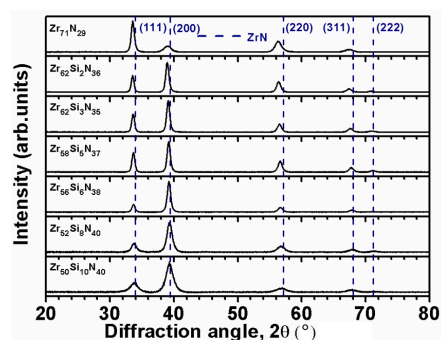
Figure 5. Grazing-incident X-ray diffraction (GIXRD) patterns of Zr–Si–N films prepared using various RF powers on Si target.
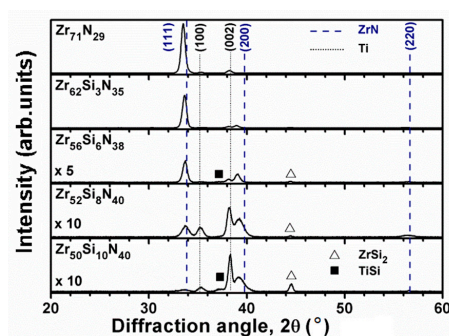

Figure 6. Bragg–Brentano scan X-ray diffraction (XRD) patterns of Zr–Si–N films with a Ti interlayer.
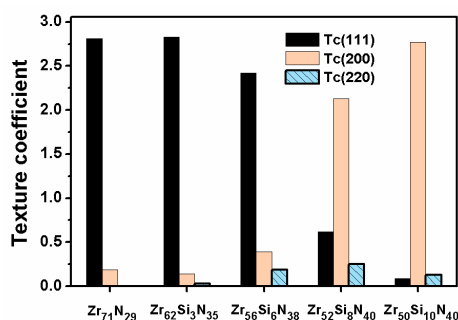

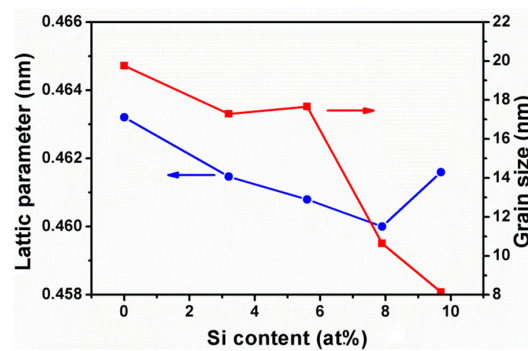**Figure 7.** Texture coefficients of Zr–Si–N films with various Si contents.

Figure 8. Lattice parameters and grain sizes of the Zr–Si–N films.

Figures 9a, 10a and 11a show the cross-sectional TEM images of the $Zr_{71}N_{29}$, $Zr_{62}Si_3N_{35}$ and $Zr_{50}Si_{10}N_{40}$ films, respectively. The selected area electron diffraction (SAED) patterns of the $Zr_{71}N_{29}$ and $Zr_{62}Si_3N_{35}$ films in Figures 9a and 10a indicated a fcc ZrN phase, while the SAED pattern of the $Zr_{50}Si_{10}N_{40}$ films consisted of continuous rings, which implies a nanostructure. The high-magnification images of the $Zr_{71}N_{29}$ and $Zr_{62}Si_3N_{35}$ films (Figures 9b and 10b) exhibited a columnar structure with widths of 19–22 and 14–17 nm, respectively. Figure 11b shows that the $Zr_{50}Si_{10}N_{40}$ films exhibits a fine structure and the width of the short columnar structure narrows to 9 nm only. The widths of the columnar structure in the Zr–Si–N films displayed a decreasing trend with increasing the Si content, which were consistent with the calculated grain sizes from XRD evaluation (Figure 8). Moreover, the short columnar structure of the $Zr_{50}Si_{10}N_{40}$ films that represented the crystalline regions were interrupted by amorphous tissue in the growth direction. Therefore, the lattice parameters of the $Zr_{50}Si_{10}N_{40}$ films did not follow the variation tendency of the Zr–Si–N films with 0–8 at.% Si, and the solid solution strengthening by introducing Si into ZrN matrix were negligible for the $Zr_{50}Si_{10}N_{40}$ films.
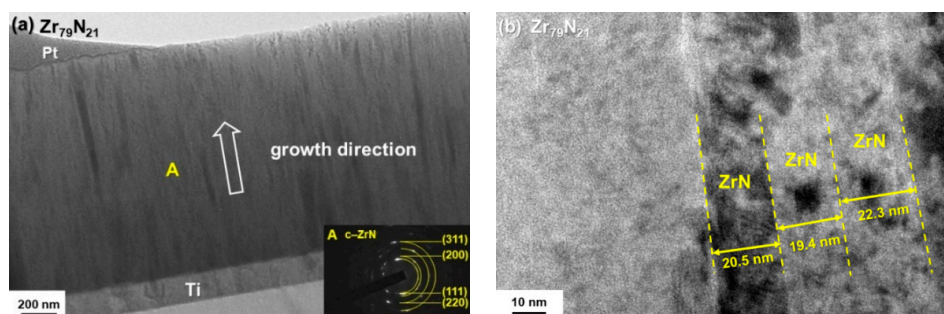

Figure 9. (**a**) Cross-sectional transmission electron microscopy (TEM) image and selected area electron diffraction (SAED) pattern and (**b**) high-magnification TEM image of the $Zr_{71}N_{29}$ films.
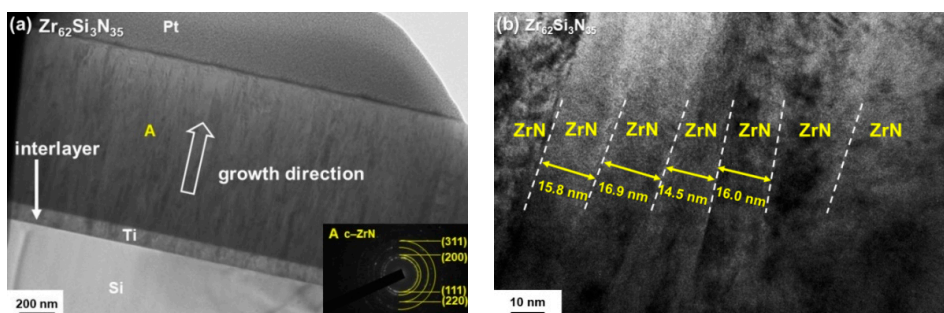

Figure 10. (**a**) Cross-sectional TEM image and SAED pattern and (**b**) high-magnification TEM image of the $Zr_{62}Si_3N_{35}$ films.

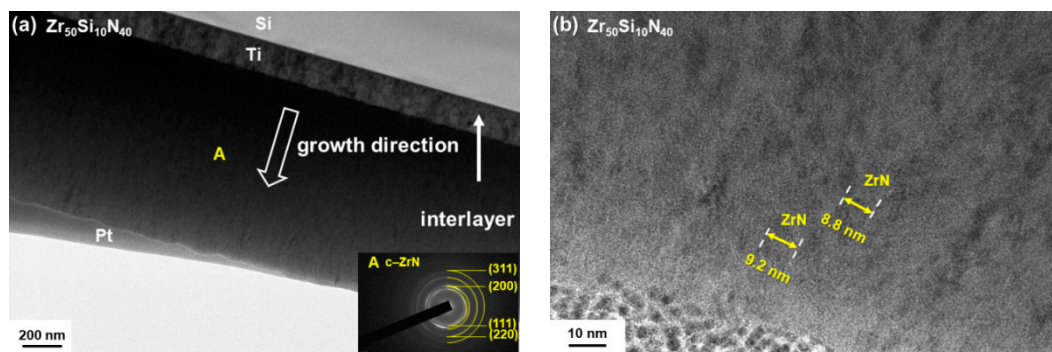**Figure 11.** (**a**) Cross-sectional TEM image and SAED pattern and (**b**) high-magnification TEM image of the $Zr_{50}Si_{10}N_{40}$ films.

Table 2 and Figure 12 shows the hardness and residual stresses of the Zr–Si–N films with various Si contents. The $Zr_{71}N_{29}$ films exhibited a hardness of 21.5 GPa and a low compressive residual stress of −0.6 GPa, while the hardness were 33.1–34.3 GPa for the films with 2–6 at.% Si. This was accompanied with an elevated compressive residual stress level from −4.4 to −5.0 GPa. A further increase in Si content to 8 and 10 at.% resulted in decreased hardness of 27.4 and 21.5 GPa, respectively, which was accompanied with a decrease in the residual stress values to −2.8 and −1.8 GPa, respectively. The low-Si-content films exhibited a solid solution strengthening effect, while the formation of amorphous Si_3N_4 for high-Si-content films decreased the mechanical properties and relaxed the residual stress. Most of the previous studies on Zr–Si–N films reported a maximum hardness, which was accompanied with a certain range of Si contents [7–10]. Dong et al. [10], Martin et al. [9] and Mae et al. [8] reported maximum hardness of 29.8 GPa at 6.2 at.% Si, 36 GPa at 2 at.% Si and 35 GPa at 3 at.% Si, respectively. In the study conducted by Martin et al. [9], the films with a hardness of 36 GPa exhibited a stress of −5.7 GPa and a grain size of 17 nm. These characteristics seemed similar to the reported data in this study. The variation of hardness was evidently related to that of the residual stress [8,14]. Figure 13a shows the relationship of hardness and residual stress for Batches I and II samples, which exhibits a linear trend except for the hardness of $Zr_{71}N_{29}$ films. A similar linear relationship between Young's modulus and residual stress was shown in Figure 13b. Table 2 shows that the Zr–Si–N films with 2–6 at.% Si shows high H^3/E^2 levels of 0.26–0.30 GPa, which was accompanied with low roughness levels of 0.8–1.4 nm.
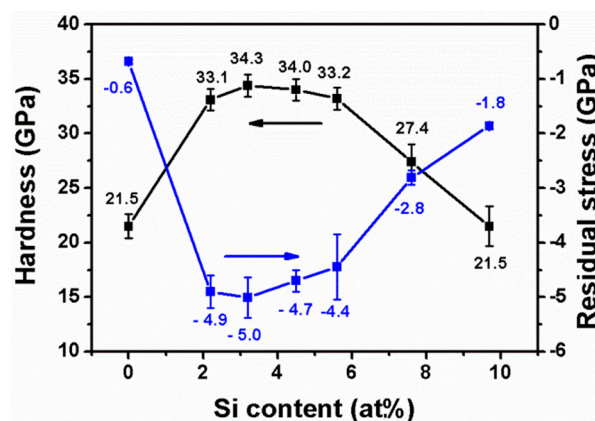

Figure 12. Nanoindentation hardness and residual stress values of Zr–Si–N films.
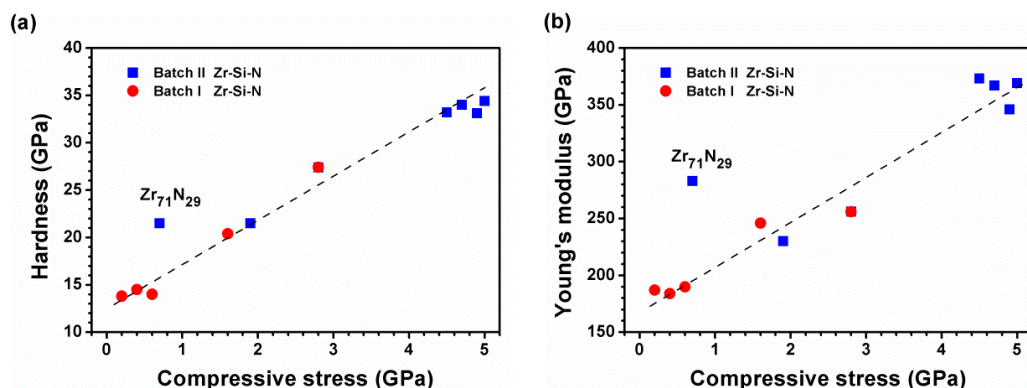
Figure 13. The relationships of (**a**) nanoindentation hardness and (**b**) Young's modulus of Zr–Si–N films to their residual stress values.

4. Conclusions

Under-stoichiometric Zr–Si–N films with atomic ratios N/(Zr + Si) of 0.41–0.89 were fabricated through HiPIMS/RFMS co-sputtering. The structural characteristics of Zr–Si–N films was influenced by their constitutions. The films with Si content of less than 9 at.% and N content of less than 43 at.% displayed a face-centered cubic structure. The mechanical properties of Zr–Si–N films exhibited linear tendencies that were related to their residual stresses. The crystalline Zr–Si–N films of 2–6 at.% Si showed a high nanoindentation hardness level of 33.1–34.3 GPa and a high Young's modulus level of 346–373 GPa, which demonstrated H^3/E^2 values of 0.26–0.30 GPa and surface roughness of 0.8–1.4 nm.

References

1.   Vepřek, S.; Haussmann, M.; Reiprich, S.; Li, S.; Dian, J. Novel thermodynamically stable and oxidation resistant superhard coating materials. *Surf. Coat. Technol.* **1996**, *86–87*, 394–401. [CrossRef]

2.   Veprek, S.; Niederhofer, A.; Moto, K.; Bolom, T.; Männling, H.-D.; Nesladek, P.; Dollinger, G.; Bergmaier, A. Composition, nanostructure and origin of the ultrahardness in *nc*-TiN/a-Si$_3$N$_4$/a- and *nc*-TiSi$_2$ nanocomposites with H_V = 80 to ≥105 GPa. *Surf. Coat. Technol.* **2000**, *133–134*, 152–159. [CrossRef]

3.   Diserens, M.; Patscheider, J.; Lévy, F. Mechanical properties and oxidation resistance of nanocomposite TiN–SiN$_x$ physical-vapor-deposited thin films. *Surf. Coat. Technol.* **1999**, *120–121*, 158–165. [CrossRef]

4.   Vaz, F.; Rebouta, L.; Goudeau, P.; Pacaud, J.; Garem, H.; Rivière, J.P.; Cavaleiro, A.; Alves, E. Characterisation of Ti$_{1−x}$Si$_x$N$_y$ nanocomposite films. *Surf. Coat. Technol.* **2000**, *133–134*, 307–313. [CrossRef]

5.   Benkahoul, M.; Sandu, C.S.; Tabet, N.; Parlinska-Wojtan, M.; Karimi, A.; Lévy, F. Effect of Si incorporation on the properties of niobium nitride films deposited by DC reactive magnetron sputtering. *Surf. Coat. Technol.* **2004**, *188–189*, 435–439. [CrossRef]

6.   Sandu, C.S.; Benkahoul, M.; Sanjinés, R.; Lévy, F. Model for the evolution of Nb–Si–N thin films as a function of Si content relating the nanostructure to electrical and mechanical properties. *Surf. Coat. Technol.* **2006**, *201*, 2897–2903. [CrossRef]

7.   Sandu, C.S.; Sanjinés, R.; Benkahoul, M.; Medjani, F.; Lévy, F. Formation of composite ternary nitride thin films by magnetron sputtering co-deposition. *Surf. Coat. Technol.* **2006**, *201*, 4083–4089. [CrossRef]

8. Mae, T.; Nose, M.; Zhou, M.; Nagae, T.; Shimamura, K. The effects of Si addition on the structure and mechanical properties of ZrN thin films deposited by an r.f. reactive sputtering method. *Surf. Coat. Technol.* **2001**, *142–144*, 954–958. [CrossRef]

9. Martin, P.J.; Bendavid, A.; Cairney, J.M.; Hoffman, M. Nanocomposite Ti–Si–N, Zr–Si–N, Ti–Al–Si–N, Ti–Al–V–Si–N thin film coatings deposited by vacuum arc deposition. *Surf. Coat. Technol.* **2005**, *200*, 2228–2235. [CrossRef]

10. Dong, Y.; Zhao, W.; Li, Y.; Li, G. Influence of silicon on the microstructure and mechanical properties of Zr–Si–N composite films. *Appl. Surf. Sci.* **2006**, *252*, 5057–5062. [CrossRef]

11. Choi, H.; Jang, J.; Zhang, T.; Kim, J.H.; Park, I.W.; Kim, K.H. Effect of Si addition on the microstructure, mechanical properties and tribological properties of Zr–Si–N nanocomposite coatings deposited by a hybrid coating system. *Surf. Coat. Technol.* **2014**, *259*, 707–713. [CrossRef]

12. Chen, Y.I.; Lin, K.Y.; Wang, H.H.; Cheng, Y.R. Characterization of Ta–Si–N coatings prepared using direct current magnetron co-sputtering. *Appl. Surf. Sci.* **2014**, *305*, 805–816. [CrossRef]

13. Chen, Y.I.; Gao, Y.X.; Chang, L.C.; Ke, Y.E.; Liu, B.W. Mechanical properties, bonding characteristics, and oxidation behaviors of Nb–Si–N coatings. *Surf. Coat. Technol.* **2018**, in press. [CrossRef]

14. Chen, Y.I.; Chang, S.C.; Chang, L.C. Oxidation resistance and mechanical properties of Zr–Si–N coatings with cyclic gradient concentration. *Surf. Coat. Technol.* **2017**, *320*, 168–173. [CrossRef]

15. Chen, Y.I.; Cheng, Y.R.; Chang, L.C.; Lu, T.S. Chemical inertness of Ta–Si–N coatings in glass molding. *Thin Solid Films* **2015**, *584*, 66–71. [CrossRef]

16. Chang, L.C.; Zheng, Y.Z.; Chen, Y.I.; Chang, S.C.; Liu, B.L. Bonding characteristics and chemical inertness of Zr–Si–N coatings with a high Si content in glass molding. *Coatings* **2018**, *8*, 181. [CrossRef]

17. Kouznetsov, V.; Macák, K.; Schneider, J.M.; Helmersson, U.; Petrov, I. A novel pulsed magnetron sputter technique utilizing very high target power densities. *Surf. Coat. Technol.* **1990**, *122*, 290–293. [CrossRef]

18. Helmersson, U.; Lattemann, M.; Bohlmark, J.; Ehiasarian, A.P.; Gudmundsson, J.T. Ionized physical vapor deposition (IPVD): A review of technology and applications. *Thin Solid Films* **2006**, *513*, 1–24. [CrossRef]

19. Purandare, Y.P.; Ehiasarian, A.P.; Hovsepian, P.E. Structure and properties of ZrN coatings deposited by high power impulse magnetron sputtering technology. *J. Vac. Sci. Technol. A* **2011**, *29*, 011004. [CrossRef]

20. Ehiasarian, A.P.; Münz, W.-D.; Hultman, L.; Helmersson, U.; Petrov, I. High power pulsed magnetron sputtered CrN$_x$ films. *Surf. Coat. Technol.* **2003**, *163*, 267–272. [CrossRef]

21. Greczynski, G.; Lu, J.; Jensen, J.; Bolz, S.; Kölker, W.; Schiffers, C.; Lemmer, O.; Greene, J.E.; Hultman, L. A review of metal-ion-flux-controlled growth of metastable TiAlN by HIPIMS/DCMS co-sputtering. *Surf. Coat. Technol.* **2014**, *257*, 15–25. [CrossRef]

22. Chang, L.C.; Chang, C.Y.; You, Y.W. Ta–Zr–N thin films fabricated through HIPIMS/RFMS co-sputtering. *Coatings* **2017**, *7*, 189. [CrossRef]

23. Chang, L.C.; Chang, C.Y.; Chen, Y.I.; Kao, H.L. Mechanical properties and oxidation behavior of ZrN$_x$ thin films fabricated through high-power impulse magnetron sputtering deposition. *J. Vac. Sci. Technol. A* **2016**, *34*, 02D107. [CrossRef]

24. Oliver, W.C.; Pharr, G.M. An improved technique for determining hardness and elastic modulus using load and displacement sensing indentation experiments. *J. Mater. Res.* **1992**, *7*, 1564–1583. [CrossRef]

25. Janssen, G.C.A.M.; Abdalla, M.M.; van Keulen, F.; Pujada, B.R.; van Venrooy, B. Celebrating the 100th anniversary of the Stoney equation for film stress: Developments from polycrystalline steel strips to single crystal silicon wafers. *Thin Solid Films* **2009**, *517*, 1858–1867. [CrossRef]

26. Audronis, M.; Bellido-Gonzalez, V.; Daniel, B. Control of reactive high power impulse magnetron sputtering processes. *Surf. Coat. Technol.* **2010**, *204*, 2159–2164. [CrossRef]

27. Purandare, Y.P.; Ehiasarian, A.P.; Hovsepian, P.E. Target poisoning during CrN deposition by mixed high power impulse magnetron sputtering and unbalanced magnetron sputtering technique. *J. Vac. Sci. Technol. A* **2016**, *34*, 041502. [CrossRef]

28. Anders, A. Tutorial: Reactive high power impulse magnetron sputtering (R-HiPIMS). *J. Appl. Phys.* **2017**, *121*, 171101. [CrossRef]

29. Tsui, T.Y.; Pharr, G.M.; Oliver, W.C.; Bhatia, C.S.; White, R.L.; Anders, S.; Anders, A.; Brown, I.G. Nanoindentation and nanoscratching of hard carbon coatings for magnetic disks. *Mater. Res. Soc. Symp. Proc.* **1995**, *383*, 447–452. [CrossRef]

30.   Cheng, H.E.; Hon, M.H. Texture formation in titanium nitride films prepared by chemical vapor deposition. *J. Appl. Phys.* **1996**, *79*, 8047–8053. [CrossRef]

31.   Jones, M.I.; McColl, I.R.; Grant, D.M. Effect of substrate preparation and deposition conditions on the preferred orientation of TiN coatings deposited by RF reactive sputtering. *Surf. Coat. Technol.* **2000**, *132*, 143–151. [CrossRef]

32.   Cullity, B.D.; Stock, S.R. *Elements of X-Ray Diffraction*, 3rd ed.; Prentice Hall: Upper Saddle River, NJ, USA, 2001.